Inorganic Chemistry
Article

Inorg. Chem. **2010**, *49*, 8457–8464 **8457**
DOI: 10.1021/ic1010192

TiO_2(B) Nanoribbons As Negative Electrode Material for Lithium Ion Batteries with High Rate Performance

Thomas Beuvier,[†] Mireille Richard-Plouet,*,[†] Maryline Mancini-Le Granvalet,[†] Thierry Brousse,[‡] Olivier Crosnier,[‡] and Luc Brohan*,[†]

[†]*Institut des Matériaux Jean Rouxel (IMN), Université de Nantes, CNRS, 2, rue de la Houssinière BP32229, F44322 NANTES Cedex, France, and* [‡]*Laboratoire de Génie des Matériaux et Procédés Associés (LGMPA-EA2664), Polytech Nantes, Université de Nantes, La Chantrerie, rue Christian Pauc, BP50609, F44306 Nantes Cedex 3, France*

Received May 20, 2010

Nanosized TiO_2(B) has been investigated as a possible candidate to replace $Li_4Ti_5O_{12}$ or graphite as the negative electrode for a Li-ion battery. Nanoribbon precursors, classically synthesized in autogenous conditions at temperatures higher than 170 °C in alkaline medium, have been obtained, under reflux ($T \sim 120$ °C, $P = 1$ bar). After ionic exchange, these nanoribbons exhibit a surface area of 140 $m^2\ g^{-1}$, larger than those obtained under autogenous conditions or by solid state chemistry. These nanoparticles transform after annealing to isomorphic titanium dioxide. They mainly crystallize as the TiO_2(B) variety with only 5% of anatase. This quantification of the anatase/TiO_2(B) ratio was deduced from Raman spectroscopy measurement. TEM analysis highlights the excellent crystallinity of the nanosized TiO_2(B), crystallizing as 6 nm thin nanoribbons. These characteristics are essential in lithium batteries for a fast lithium ion solid state diffusion into the active material. In lithium batteries, the TiO_2(B) nanoribbons exhibit a good capacity and an excellent rate capability (reversible capacity of 200 mA h g^{-1} at C/3 rate (111 mA g^{-1}), 100 mA h g^{-1} at 15C rate (5030 mA g^{-1}) for a 50% carbon black loaded electrode). The electrode formulation study highlights the importance of the electronic and ionic connection around the active particles. The cycleability of the nano-TiO_2(B) is another interesting point with a capacity loss of 5% only, over 500 cycles at 3C.

Introduction

Among insertion compounds used as a lithium-ion battery negative electrode, TiO_2(B) has been investigated as a promising material for lithium storage.[1] It retains the advantages of $Li_4Ti_5O_{12}$ with low cost, low toxicity, and high safety and presents moreover a higher theoretical capacity (335 mA h g^{-1} instead of 175 mA h g^{-1} for $Li_4Ti_5O_{12}$)[2−5] close to the graphite one (372 mA h g^{-1}).[6] It has been recently reported that TiO_2(B) nanoparticles have a high reversible capacity, in the range of 200−300 mA h g^{-1} with good cycleability.[7] Moreover the lithium insertion/deinsertion inside the host TiO_2(B) lattice is dictated by a pseudocapacitive behavior thus contributing to its large power density.[8]

TiO_2(B) nanoparticles, which can improve the insertion/deinsertion rate, were synthesized by various research teams[9−12] reproducing Kasuga's synthesis[13] and using reaction between NaOH and TiO_2 in autoclaves. In a typical synthesis, titanium oxide is dispersed in highly concentrated alkaline solutions, and the resulting suspension is poured into an autoclave or a reflux system for heating between 100 and 250 °C (Step 1). As recently reviewed in ref 14, this process leads to sodium titanate nanoparticles with various morphologies: nanospheres,[15] nanosheets, nanotubes (hollow cylinders), and nanofibers (rectangular bases) in which can be

---

*To whom correspondence should be addressed. E-mail: mireille.richard@cnrs-imn.fr (M.R.-P.), luc.brohan@cnrs-imn.fr (L.B.). Phone: + 33 240 37 39 56 (M.R.-P.), + 33 240 37 39 35 (L.B.). Fax: + 33 240 37 39 95 (M.R.-P.), + 33 240 37 39 95 (L.B.).

(1) Brohan, L.; Marchand, R. *Solid State Ionics* **1983**, *9−10*, 419.
(2) Murphy, D. W.; Cava, R. J.; Zahurak, S. M.; Santoro, A. *Solid State Ionics* **1983**, *9−10*, 413.
(3) Ferg, E.; Gummow, R. J.; De Kock, A.; Thackeray, M. M. *J. Electrochem. Soc.* **1994**, *141*, L147.
(4) Colbow, K. M.; Dahn, J. R.; Haering, R. R. *J. Power Sources* **1989**, *26*, 397.
(5) Brousse, T.; Fragnaud, P.; Marchand, R.; Schleich, D. M.; Bohnke, O.; West, K. *J. Power Sources* **1997**, *68*, 412.
(6) Ogumi, Z.; Inaba, M. *Bull. Chem. Soc. Jpn.* **1998**, *71*, 521.
(7) Armstrong, A. R.; Armstrong, G.; Canales, J.; Bruce, P. G. *Angew. Chem., Int. Ed.* **2004**, *43*, 2286.
(8) Zukalová, M.; Kalbáč, M.; Kavan, L.; Exnar, I.; Graetzel, M. *Chem. Mater.* **2005**, *17*, 1248.
(9) Bruce, P. G.; Scrosati, B.; Tarascon, J.-M. *Angew. Chem., Int. Ed.* **2008**, *47*, 2930.
(10) Zukalová, M.; Kalbáč, M.; Kavan, L.; Exnar, I.; Haeger, A.; Graetzel, M. *Prog. Solid State Chem.* **2005**, *33*, 253.
(11) Jitputti, J.; Suzuki, Y.; Yoshikawa, S. *Catal. Commun.* **2008**, *9*, 1265.
(12) Lan, Y.; Gao, X.; Zhu, H.; Zheng, Z.; Yan, T.; Wu, F.; Ringer, S. P.; Song, D. *Adv. Funct. Mater.* **2005**, *15*, 1310.
(13) Kasuga, T.; Hiramatsu, M.; Hosun, A.; Sekino, T.; Niihara, K. *Langmuir* **1998**, *14*, 3160.
(14) Bavykin, D. V.; Walsh, F. C. *Eur. J. Inorg. Chem.* **2009**, *8*, 977.
(15) Beuvier, T.; Richard-Plouet, M.; Brohan, L. *J. Phys. Chem. C* **2010**, *114*, 7660.

included nanorods, nanowires, nanobelts, and nanoribbons. In the following, we use the latter denomination because the thickness is smaller than 20 nm. Various factors were identified to play a major role on the morphology during the Na-titanate formation, such as TiO_2 precursor, thermal treatment, NaOH concentration, and reaction time.[16-21] In 2005, Lan and co-workers[12] have explored the influence of reaction temperature and treatment time. They reported that nanotubes are formed after hydrothermal treatment of TiO_2 particles in 10 mol L^{-1} NaOH solution at 150 °C for 24 h, whereas nanoribbons appeared at higher temperature (180 °C). The titanium concentration in suspension was not specified despite its importance according to Bavykin et al.[22] The latter team also studied the impact of temperature and alkaline concentration. By setting the reaction time to 22 h, they found that, raising the temperature from 120 to 150 °C results in an increase in the nanotube diameter, and at a temperature above 170 °C, non-porous nanoribbons are formed. These results were obtained by processing 1 g of TiO_2 anatase precursor in 300 mL of NaOH, 10 mol L^{-1}. Morgan et al.[23] proposed a morphology phase diagram based on temperature and NaOH concentration after hydrothermal treatment for 20 h. They observed that high temperature and high NaOH concentration facilitate nanoribbon formation. When the temperature was elevated above 180 °C and for NaOH concentration equal to 10 mol L^{-1}, a phase transition between nanotubes to nanoribbons was observed in agreement with the works of Bavykin and Lan. According to the recent literature, TiO_2(B) nanoribbons seem to be synthesized only by hydrothermal treatment at temperatures above 170 °C. They are more crystallized than nanotubes and generally produce titanium dioxide with the highest proportion of TiO_2(B). In addition, their surface area[8,24] is higher (~30 $m^2\ g^{-1}$) when nanoribbons are obtained from titanates synthesized by solid state chemistry (< 10 $m^2\ g^{-1}$),[5,8] but it remains lower when TiO_2 is obtained from nanotubes.[14,25] Using reflux instead of autoclaving mainly leads to nanotubes that further transform as anatase. The challenge for higher surface area with pure TiO_2(B) variety consists in synthesizing smaller nanoribbons than those synthesized by autogenous treatment. Therefore, we investigate this possibility by using a reflux method.

In a first part, we report the synthesis of titanic acid as nanoribbons and their characterization. They are obtained by ionic exchange in an acidic solution of Na-titanate nanoribbons obtained by refluxing at 120 °C. In a second part, the annealing effect on the titanic acid transformation to nanosized TiO_2(B) was studied to optimize the crystallinity and the electrochemical performance. In a last part, high charge/discharge rates were tested on TiO_2(B) electrodes in lithium half cells by investigating the electrode preparation.

Experimental Section

Precursor. The titanium oxide hydrate precursor, $TiO_2\cdot 2H_2O$ is obtained by precipitation, starting from $TiOCl_2$ solution (4.85 mol L^{-1} in HCl, Millenium) and an excess of 12.5 wt % NH_3, aq (SDS). The white precipitate is rinsed with deionized water, filtered, and finally dried at 70 °C in air.

Refluxing Treatment (Step 1) and Ionic Exchange (Step 2). Sodium titanate was obtained by dispersing 2 g of titanium oxide precursor in 120 mL of concentrated (12 mol L^{-1}) NaOH solution. The suspension was poured in a 300 mL capacity PTFE round-bottom flask equipped with a coil reflux condenser. The preparation was kept under vigorous stirring (200 rds min^{-1}). The flask was placed in silicon oil bath and heated up to 120 °C (suspension temperature). The reaction time was fixed to 7 days. The suspension was rinsed with deionized water and then rapidly stirred in diluted acidic solutions (HNO_3, 0.1 mol L^{-1}) during 4 h allowing Na^+ ions full exchange by H^+. Then, the suspension was rinsed with deionized water until the pH > 6 and dried at 70 °C.

Further Processing (Step 3). The thermal treatment of the synthesized titanic acid was carried out in air, at 400 °C for 3 h and 24 h and at 500 °C for 3 h. The plateau temperatures were reached in 2 h.

Characterization. The isothermal adsorption/desorption curves were recorded with an ASAP 2010 system by using nitrogen gas. The Brunauer–Emmett–Teller (BET) and Barret–Joyner–Halenda (BJH) models were used to extract surface areas and pore-size distributions. Thermogravimetric analysis coupled to mass spectrometry (TGA-MS) studies were performed using a SETARAM TG-DSC 111 apparatus equipped with a Mass Spectrometer facility (Leybold Inficon). The experiments were performed by heating from 25 to 1000 at 5 °C min^{-1}, in Ar environment. FT-Raman spectra were recorded on a Bruker RFS100 spectrometer equipped with a 1064 nm laser as incident light, which allows one to focus a sample area with a diameter smaller than 1 mm. The average power at the surface was around 100 mW. X-ray diffraction (XRD) patterns were collected in transmission mode, on an INEL diffractometer, with a Cu anode as X-ray source (λ = 1.54059 Å), equipped with a curved detector, ranging from 0 to 120°. The powders were set in a Lindeman glass capillary (0.3 mm diameter). Rietveld refinements were conducted with the Jana2006 program suite.[26] The experimental peak width was calculated using the fundamental parameters of the X-ray diffractometer. Transmission electron microscopy (TEM) studies were carried out on a Hitachi HNAR9000 with a LaB_6 thermo-ionic emission electron source operating at 300 kV. The sample, annealed at 500 °C for 3 h, was ground, dispersed in distilled water, and finally a drop was evaporated on holey carbon films on copper grids for TEM observations. TEM simulations were performed with Mac Tempas program[27] using TiO_2(B) structure parameters,[28] including cell parameters, space group, atom positions together with thickness and defocalization. Electrochemical experiments were performed with a Mac-Pile equipment (BioLogic), using a two-electrode cell configuration with metallic lithium as both the counter and the reference electrode.

---

(16) Kolen'ko, Y. V.; Kovnir, K. A.; Gavrilov, A. I.; Garshev, A. V.; Frantti, J.; Lebedev, O. I.; Churagulov, B. R.; Van Tendeloo, G.; Yoshimura, M. *J. Phys. Chem. B* **2006**, *110*, 4030.

(17) Bavykin, D. V.; Friedrich, J. M.; Walsh, F. C. *Adv. Mater.* **2006**, *18*, 2807.

(18) Wei, M.; Qi, Z.-M.; Ichihara, M.; Honma, I.; Zhou, H. *Chem. Phys. Lett.* **2006**, *424*, 316.

(19) Daoud, W. A.; Pang, G. K. H. *J. Phys. Chem. B* **2006**, *110*, 25746.

(20) Zarate, R. A.; Fuentes, S.; Wiff, J. P.; Fuenzalida, V. M.; Cabrera, A. L. *J. Phys. Chem. Solids* **2007**, *68*, 628.

(21) Papa, A. L.; Millot, N.; Saviot, L.; Chassagnon, R.; Heintz, O. *J. Phys. Chem. C* **2009**, *113*, 12682.

(22) Bavykin, D. V.; Parmon, V. N.; Lapkin, A. A.; Wamsh, F. C. *J. Mater. Chem.* **2004**, *14*, 3370.

(23) Morgan, D. L.; Zhu, H.-Y.; Frost, R. L.; Waclawik, E. R. *Chem. Mater.* **2008**, *20*, 3800.

(24) Armstrong, G.; Armstrong, A. R.; Bruce, P. G.; Reale, P.; Scrosati, B. *Adv. Mater.* **2006**, *18*, 2597.

(25) Yu, J.; Yu, H. *Mater. Chem. Phys.* **2006**, *100*, 507.

(26) Petricek, V.; Dusek, M.; Palatinus, L. *Jana2006, The crystallographic computing system*; Institute of Physics: Praha, Czech Republic, 2006.

(27) O'Keefe, M. A.; Kilaas, R. *MacTempas, V1.70 and Crystalkit V1.77, HRTEM Image Analysis*; Lawrence Berkley National Laboratory: Berkeley, CA, 1987.

(28) Ben Yahia, M.; Lemoigno, F.; Beuvier, T.; Filhol, J.-S.; Richard-Plouet, M.; Brohan, L.; Doublet, M.-L. *J. Chem. Phys.,* **2009**, *130*, 204501.

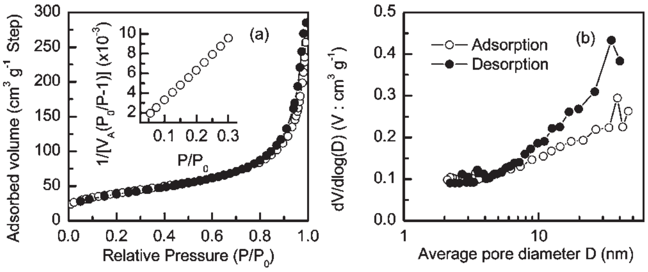

Figure 1. (a) Nitrogen adsorption−desorption isotherms of titanic acid nanoribbons. The inset refers to the BET specific surface area analysis. (b) BJH pore size distribution between 2 and 50 nm. Open and filled circles refer to adsorption and desorption isotherms.

Composite electrodes were prepared by mixing TiO_2, acetylene black, and poly(vinylidene fluoride) (PVDF) dissolved in NMP (*N*-Methyl-2-pyrrolidone) in the following weight ratio: 70:24:6 (except in the last part of our study where a 44:50:6 ratio was tested). Acetylene black is added as a conductive additive, and PVDF acts as a binder for keeping the mechanical integrity of the electrode. Copper-foil disks were cut off and used as current collector substrates (0.85 cm^2) on which 2.0−3.0 mg of active material were deposited. The electrolyte used was 1 mol L^{-1} $LiPF_6$ solution in ethylene carbonate:diethyl carbonate (Merck), with a volume ratio of 1:1. A glass fiber paper was used as the separator and was impregnated with the electrolyte solution. The C-rate was defined by $C = I_A/Q_{Th}$, where I_A is the applied current (mA g^{-1}) and Q_{Th} is the theoretical capacity for one lithium per TiO_2 unit (i.e., $Q_{Th} = 335$ mA h g^{-1}).

Results and Discussion

Annealing Investigation. Titanic Acid. The isotherm for nitrogen adsorption/desorption on the titanic acid surface is shown in Figure 1a. It is characteristic of non-porous particles[14,18] with strong interaction between N_2 and titanic acid. The gas adsorption in the $P/P_0 = 0.1-0.3$ range, quite close to the monolayer adsorption, gives a specific surface area of 140 m^2 g^{-1} calculated by the BET equation (Figure 1a, inset). The pore size distribution determined by the BJH method is shown in Figure 1b. The absence of a peak below 10 nm indicates the absence of porous nanotubes.

In Figure 2a, the TEM analysis reveals the presence of non-porous nanoribbons: around 30 nm large and 1−2 μm long. Thus, the formation of nanoribbons is not limited to hydrothermal process but is also possible under reflux at 120 °C (boiling temperature of the concentrated NaOH solution) as already reported.[15] The long reaction time (7 days) explains the appearance of this morphology. A high resolution image is shown in Figure 2b. Its Fourier transform is presented in the inset. The spots can not be indexed using one of the two classically reported structures for titanic acids ($H_2Ti_3O_7$[29,30] and pseudolepidocrocite[31,32]). The Fourier transform is very close to the diffraction pattern of TiO_2(B) oriented along the *c*-axis. Therefore, we assume that the titanic acid has begun its transformation into TiO_2(B) because of the oxolation process and the water release in the microscope. Note that the titanic acid transforms into TiO_2(B) before 300 °C in air at normal pressure (Supporting Information, Figure S1). This temperature is low and highlights the reactivity of the titanic acid. However, the large spots in the Fourier transform give evidence of the disorder involved by partial dehydration.

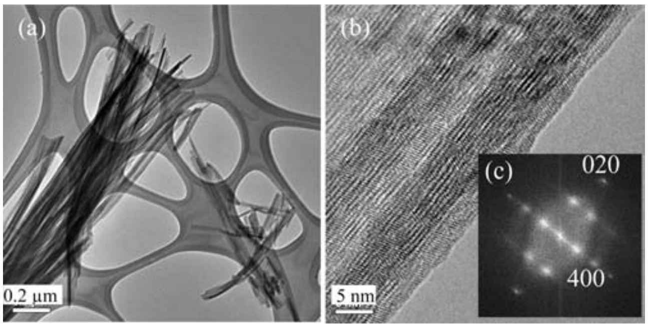

Figure 2. TEM studies of the titanic acid with nanoribbon morphology: (a) low resolution image, (b) high resolution image, and (c) FFT of the image (b). Indexes are those of TiO_2(B) oriented along the [001]* zone axis.

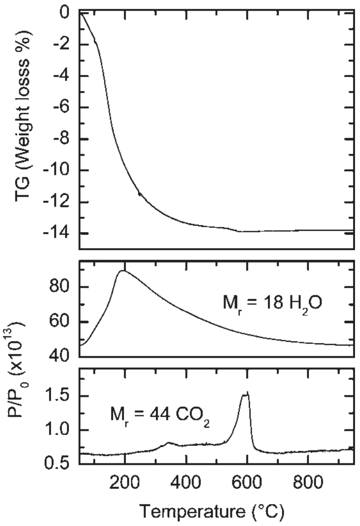

Figure 3. TGA-MS data of titanic acid.

The TGA-MS is shown in Figure 3. Two temperature zones were identified. The weight loss of 13.6% from room temperature to around 525 °C is due to release of water originating from the particle surface and from the intersheet space of the lamellar nanoribbons. Between 525 and 635 °C, a further weight loss of 0.14% is observed corresponding to CO_2 desorption. Its incorporation to the solid certainly took place during the synthesis of the Na titanate by reaction of atmospheric CO_2 with the highly alkaline solution used during the reflux synthesis. We infer that it is incorporated during this step because even washing with nitric acid after synthesis is not efficient to remove it. In addition its release takes place at high temperature, indicating that it is strongly bound to the solid. Assuming that the formulation at the end of the TG analysis is TiO_2, the deduced titanic acid formulation is $TiO_2(H_2O)_{0.70}(CO_2)_{0.003}$ or $(H_3O^+)_{0.35}TiO_2(OH^-)_{0.35}$-$(CO_2)_{0.003}$, taking into account the acidic character of the solid. Presumably, heating the titanic acid at 400 °C will lead to some residual water molecules which may have a strong impact in a non-aqueous storage device. This point will be treated in the second part of the annealing investigation.

---

(29) Feist, T. P.; Davies, O. K. *J. Solid State Chem.* **1992**, *101*, 275.
(30) Chen, Q.; Zhou, W.; Du, G.; Peng, L. M. *Adv. Mater.* **2002**, *14*, 1208.
(31) Ma, R.; Bando, Y.; Sasaki, T. *Chem. Phys. Lett.* **2003**, *380*, 577.
(32) Peng, C.-W.; Richard-Plouet, M.; Ke, T.-Y.; Chiu, H.-T.; Marhic, C.; Puzenat, E.; Lemoigno, F.; Brohan, L. *Chem. Mater.* **2008**, *20*, 7228.

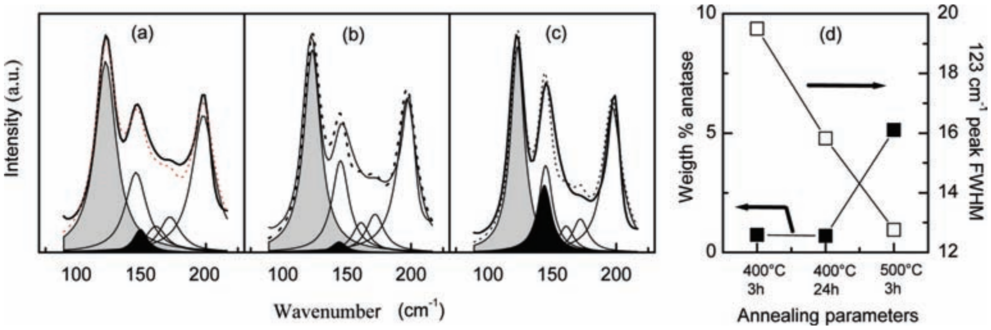

Figure 4. Raman spectra for $TiO_2(B)$ originating from the titanic acid annealed at (a) 400 °C for 3 h, (b) 400 °C for 24 h, and (c) 500 °C for 3 h. Gray and black areas correspond to the most intense peaks of $TiO_2(B)$ and anatase, respectively. The other opened areas are attributed to $TiO_2(B)$. Dotted lines correspond to fitted curves. (d) Weight percentage of anatase for the three samples deduced from Raman spectroscopy (filled squares, left-hand side axis) and the 123 cm^{-1} $TiO_2(B)$ vibration full width at half-maximum, fwhm (open squares, right-hand side axis).

$TiO_2(B)$ Crystallinity. Since the thermal treatment, via its temperature and its duration time, can greatly affect the $TiO_2(B)$ nanoribbon crystallinity, three annealing treatments were tested at 400 °C for 3 h and 24 h and at 500 °C for 3 h. The Raman spectra of the three samples are depicted between 90 and 216 cm^{-1} in Figure 4a−c. They are characteristic of the $TiO_2(B)$ variety with five scattering diffusion active modes located at 123, 145, 161, 172, and 196 cm^{-1}. Compared with the previously reported Raman spectra for pure $TiO_2(B)$,[33] the intensity of the 145 cm^{-1} vibration is enhanced, suggesting the presence of anatase whose most intense peak is located at 144 cm^{-1}. By fitting the relative intensity of the 123 cm^{-1} $TiO_2(B)$ peak and the 144−145 cm^{-1} dual anatase/TiO_2-(B) peak, it was demonstrated that the Raman spectra analysis permits an accurate quantification of the TiO_2-(B)/anatase ratio (Figure 4d).[33] It appears that the anatase weight percentages are very low: around 1(1)% for the samples annealed at 400 °C and 5(1)% for the sample annealed at 500 °C for 3 h. According to our previous work,[15] (1) the presence of $TiO_2(B)$ is due to the transformation of titanic acid with a nanoribbon morphology, (2) the presence of 1% of anatase at 400 °C is due to the presence of nanospheres in the titanic acid, and (3) the additional anatase appearing between 400 and 500 °C is due to the presence of nanotube impurities estimated here to be equal to 4%. As already reported,[15] the deduced position of the titanic acid can be set in a ternary morphological diagram (Supporting Information, Figure S2) with 96%, 4%, and 1% of nanoribbons, nanotubes, and nanospheres, respectively. These analyses prove the low impurities level of nanospheres and nanotubes mixed with the nanoribbons. In addition, as shown in Figure 4d, the full width at half-maximum (fwhm) of the 123 cm^{-1} peak decreases with temperature and plateau duration. This may account for an increase in the coherent domains in the nanocrystallites which was confirmed by the following XRD study.

The crystal structure was monitored by XRD (Figure 5). All peaks are attributed to the $TiO_2(B)$ variety. TiO_2 anatase is hardly detected first of all because of its low weight proportion (1 and 5%) and second because its (101) and (200) major peaks at $2\theta = 25.4°$ and $2\theta = 48.1°$ are very close to the (110) and (020) diffraction peaks of $TiO_2(B)$, respectively. Moreover, we observe a narrowing of the $TiO_2(B)$ peaks with thermal treatment in agreement with the increase in the crystallite size deduced from Raman spectroscopy studies. The sample annealed at 500 °C for 3 h surprisingly exhibits narrow peaks despite its high surface area (115 m^2 g^{-1}). A Rietveld refinement was performed from its XRD data, starting from the newly refined structure for $TiO_2(B)$.[28] Despite the good quality of the experimental data for nano-$TiO_2(B)$, the Rietveld refinement including $TiO_2(B)$, as a single phase, was not totally satisfactory. In particular, residues appeared as shoulders of the (110) and (020) reflection peaks, thus indicating that some amount of anatase was detected. Therefore, both phases were taken into account and their phase volume was refined to get an estimation of their proportion (Supporting Information, Figure S3, Table S1). Using this technique, the anatase amount could be estimated to 9.8(1.6)%, for the titanic acid annealed at 500 °C. Despite that this value is higher than the one obtained from Raman spectra, it has to be noted that the fit is not perfect and consequently, the quantification deduced from Raman spectroscopy (5(1)%) seems more reliable. Because of the nanometric dimensions of the materials, the particle sizes were also refined to correctly fit the peaks' broadening: anisotropy along the *b*-axis of $TiO_2(B)$ was introduced to account for the more narrow (020) peak. The particle size, reaching 20 nm along this particular direction, is only 10 nm perpendicularly. Because the experimental diagram shows a low signal to background ratio, the difference between experimental and calculated patterns is not perfectly flat. But the refinement proves the presence of anatase in the preparation, and the anisotropy along *b* was confirmed for $TiO_2(B)$, as supported by the following TEM study. These results demonstrate that combining Raman spectroscopy in the

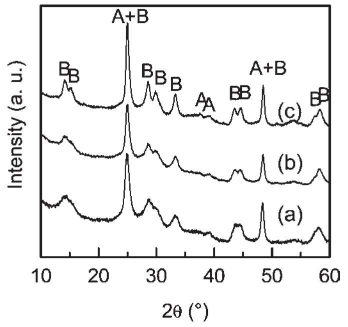

Figure 5. XRD patterns of $TiO_2(B)$ originating from titanic acid annealed at (a) 400 °C for 3 h, (b) 400 °C for 24 h, (c) 500 °C for 3 h. "A" and "B" refer to TiO_2 anatase and $TiO_2(B)$ diffraction peaks, respectively.

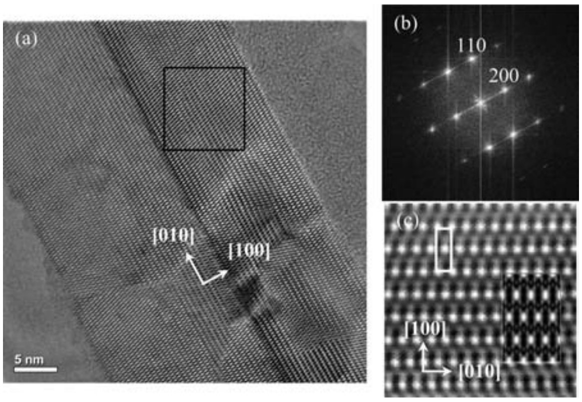

Figure 6. TEM studies of nanosized TiO_2(B) coming from the titanic acid annealed at 500 °C for 3 h: (a) high resolution image of a TiO_2(B) nanoribbon; (b) FFT of HRTEM image showing the [001]* zone axis. (c) Enlarged and filtered high resolution image along [001]*; Insets: representative unit cell marked as a white rectangle and HRTEM simulated Image (defocus −90 nm, thickness 6 nm).

range 100−250 cm^{-1} and XRD is useful to ascertain the purity of nano-TiO_2.

A typical high resolution TEM image of the sample annealed at 500 °C for 3 h, shown in Figure 6a, clearly reveals that the TiO_2(B) crystallite retains the nanoribbon morphology. The width is around 30 nm for a length of about 1−2 μm (see SEM image in the Supporting Information, Figure S4). The crystallites being too small to be isolated for selected area electron diffraction, only the Fourier transform of the marked zone in Figure 6a is presented in Figure 6b. The nanoribbon is oriented along the [001]* zone axis with a growth direction parallel to the *b*-axis of the TiO_2(B) lattice. These characteristics are commonly reported in the literature for both micro-[34,35] and nano-TiO_2(B).[15,16] The low thickness and the high crystallinity of the TiO_2(B) nanoribbons explain both the brilliance and the narrowness of the peaks observed on the Fourier transform. In Figure 6c, the HRTEM simulated image, viewed along [001]* (defocus −90 nm; thickness 6 nm) superimposes well with the observed image, and no stacking faults were detected for this nanoribbon, suggesting that the phase transformation toward anatase has not yet taken place for this particular domain of the crystallite. Assuming a nanoribbon morphology, the thickness was also corroborated by analyzing the BET results. Taking into account its surface area of 115 $m^2\ g^{-1}$ and the calculated density value to 3.71, deduced from the Rietveld refinement, the estimated thickness is 6 nm. According to the excellent crystallinity of the nanometric particles, proved by XRD and TEM analysis, lithium insertion/removal is expected to be facilitated during electrochemical measurements.

Electrochemical Performance. Figure 7 displays the incremental capacity of lithium insertion into the different samples, during the first cycle at a low current rate (C/48, i.e. applied current of 7 mA g^{-1}) deduced from the charge−discharge curves (Supporting Information, Figure S5). The two pairs of peaks with formal potential between 1.5 and 1.6 V are characteristic of lithium insertion/deinsertion in TiO_2(B).[8,36] They become more narrow upon annealing. If the peak at 1.75 V in reduction (2 V in oxidation) is undoubtedly attributed to the anatase variety,[18,19] it is also often allotted to nano-TiO_2(B)[7] although there is no Li^+ insertion process at this voltage in micro-TiO_2(B).[1,31,37] Here its intensity increases when the protonated titanate is annealed at 500 °C for 3 h in agreement with the increase in anatase content detected by Raman spectroscopy and XRD investigations. Another peak centered at 1.9−2.0 V in reduction is detected only during the first cycle. Indeed, no corresponding peak is observed upon following the oxidation. This peak has already been observed,[38] and it was assigned to solid electrolyte interface (SEI) formation. In the light of the chemical analysis performed on the different samples, its origin can also be found in the presence of water or carbonate molecules or radicals which will be reduced upon the first discharge. Residual water and carbonates are indeed difficult to avoid since these titanium oxide nanomaterials are very sensitive, and even after annealing at 400 °C for 24 h or 500 °C for 3 h some weight loss is still detected by TGA from room temperature (RT) up to 800 °C (Supporting Information, Figure S6). This explanation is in agreement with the peak intensity decrease upon annealing.

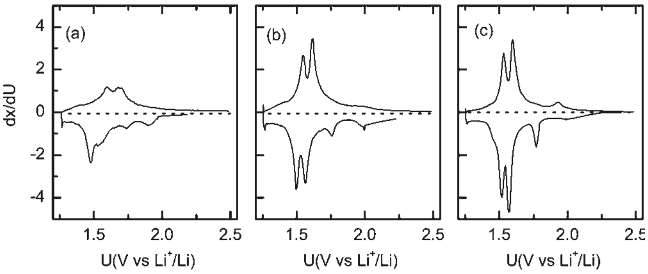

Figure 7. Incremental capacity, during the first cycle, of TiO_2(B) originating from the titanic acid annealed at (a) 400 °C for 3 h, at (b) 400 °C for 24 h, and at (c) 500 °C for 3 h. The applied current was 7.0 mA g^{-1} (C/48). The samples were cycled in 1 M $LiPF_6$ EC/DEC 1:1 electrolyte versus metallic lithium electrode.

The capacity in reduction increases from (a) to (c) with 197, 269, and 284 mA h g^{-1}, respectively, which correspond to $x = 0.59, 0.80$, and 0.84 in Li_xTiO_2(B). Thus this suggests that the higher the temperature of the thermal treatment is, the higher is the inserted lithium content. There is not much difference regarding TiO_2(B) capacities when the annealing is performed at 400 °C for 24 h or at 500 °C for 3 h. Furthermore, the polarization between the reduction and the oxidation is lower from (a) to (c). Subsequently, it can be assumed that the increase in capacity and the decrease in polarization with thermal treatment is due not only to the decrease in water content in TiO_2(B) but also to the enhancement of crystallinity. It seems reasonable to think that both factors play an important role in the lithium insertion/deinsertion processes. For that reason, a more accurate electrochemical study has

---

(33) Beuvier, T.; Richard-Plouet, M.; Brohan, L. *J. Phys. Chem. C* **2009**, *113*, 13703.

(34) Brohan, L.; Verbaere, A.; Tournoux, M.; Demazeau, G. *Mater. Res. Bull.* **1982**, *17*, 355.

(35) Tournoux, M.; Marchand, R.; Brohan, L. *Prog. Solid State Chem.* **1986**, *17*, 33.

(36) Zhang, H.; Li, G. R.; An, L. P.; Yan, T. Y.; Gao, X. P.; Zhu, H. Y. *J. Phys. Chem. C* **2007**, *111*, 6143.

(37) Brousse, T.; Marchand, R.; Taberna, P.-L.; Simon, P. *J. Power Sources* **2006**, *158*, 571.

(38) Armstrong, G.; Armstrong, A. R.; Canales, J.; Bruce, P. G. *Electrochem. Solid-State Lett.* **2006**, *9*, A139.

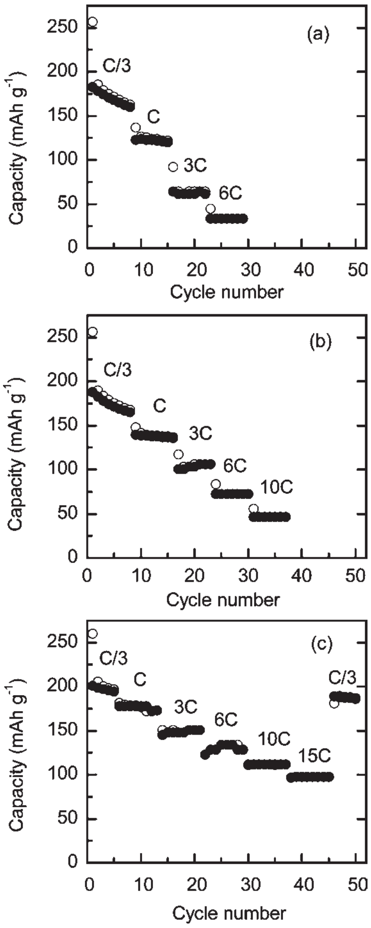

Figure 8. Variation in charge (open circles) and discharge (filled circles) at different cycling rates (Current loading of 111 mA g^{-1} (C/3) to 5030 mA g^{-1} (15C)) performed on TiO_2(B) nanoribbons annealed at 500 °C during 3 h with three different electrode preparations. The TiO_2(B)/carbon black/PVDF compositions are (a) 70:24:6, (b) 70:24:6, (c) 44:50:6 in weight ratio. The difference between (a) and (b) is that electrode (b) is pressed at 8.0 kbar. The cells were cycled in the 1.25−2.5 voltage range in 1 M $LiPF_6$ EC/DEC 1:1 electrolyte versus a metallic lithium electrode. Capacity is given per weight of TiO_2(B) active material in the electrode.

been undertaken by using the most crystallized TiO_2(B) as negative electrode material in lithium half cells.

Influence of Electrode Preparation on Rate Capability. In Figure 8 is plotted the dependence of the capacity versus the charge/discharge effective rate. The three curves refer to three different electrode preparations using titanic acid annealed at 500 °C for 3 h as active material. The results for TiO_2(B)/carbon black/PVDF composite electrode with the 70:24:6 composition (weight ratio) are presented in Figure 8a. In Figure 8b, the electrode has the same composition (70:24:6 ratio) but it has been pressed under 8.0 kbar. This pressure value is below the TiO_2(B) → anatase transformation.[34] The data for higher carbon black loaded electrode (with 44:50:6 ratio) are plotted in Figure 8c. Charge−discharge curves are shown in the Supporting Information, Figure S7. The open-circuit voltage is 3.01 V versus Li^+/Li. The initial discharge capacity, at C/3 rate (applied current of 111 mA g^{-1}) and down to 1.25 V, was quite similar for the three electrodes (256−260 mA h g^{-1}, $Li_{0.76-0.77}TiO_2$). This value is higher than that of $Li_4Ti_5O_{12}$, but comparable to the capacity of TiO_2(B) previously reported in the literature.[7,38−41] It can be noted that carbon black only accounts for 3 mA h g^{-1} (calculated for 50 wt %) because of its low double layer capacitance in the electrolyte ($\approx$15 F g^{-1} in 1 mol L^{-1} $LiPF_6$ solution in ethylene carbonate:diethyl carbonate) and was neglected in the rest of the study. A first cycle irreversible capacity loss is observed for all the samples. It can be assigned to a mix of (i) solid electrolyte interface (SEI) formation concomitant with electrolyte decomposition on the TiO_2(B) nanoribbons surface, (ii) residual CO_2 or/and H_2O adsorbed at ambient temperature in air after the annealing treatment at 500 °C, or (iii) irreversible lithium trapping in TiO_2(B) structure as it was already reported in the literature (Q_{irr} = 40−110 mA h g^{-1}).[7,37,38,40] The electrochemical Li^+ insertion/deinsertion process is reversible during the next cycles. Furthermore, the rate capability differs for the three electrodes. At the 6C rate (2010 mA g^{-1}), whereas the nonpressed electrode (70:24:6 ratio) exhibits a capacity limited to 30 mA h g^{-1}, the pressed one displays better performance since the capacity reaches 75 mA h g^{-1}. The third electrode (50% black content instead of 24%) shows the best results with high cycleability and very high rate capability. For comparison with the above-mentioned results, the capacity at 6C and 15C (5030 mA g^{-1}) is 128 and 100 mA h g^{-1}, respectively. The latter, corresponding to a charge or discharge in $\approx$1 min, is still about half of that obtained at a C/3 rate. Furthermore, after fast charge−discharge cycles, the low rate (C/3) capacity is still recovered. At the end of these 50 cycles, the capacity was measured again at different cycling rates in a larger voltage range (ΔU = 1.0−2.5 V, Figure 9). We observe a more important capacity loss than in the 1.25−2.5 V range. This may be due to irreversible Li^+ trapping in carbon below 1.25 V. Indeed, unlike for the more narrow potential window, an irreversible capacity loss is observed within the 1.0−2.5 V potential range at C/10, C/3 and even C. Irreversible trapping of lithium ions in carbon can also inhibit lithium insertion in TiO_2(B) by surface blocking.

Long-term cycling ability was also performed. The right part of the Figure 9 shows the capacity between the 89th to the 600th at 3C in the 1.25−2.5 V range. The capacity loss is very low (5%) with no incremental capacity change (Inset of Figure 9) which highlights the excellent cycleability of lithium insertion/deinsertion in TiO_2(B).

It has to be noted that the same results are obtained if an electrode with this composition (TiO_2, acetylene black and poly(vinylidene fluoride) with 44:50:6 ratio) is pressed under 8 kbar (results not shown).

To explain the performance differences between the three electrodes, the polarizations ΔU between oxidation and reduction processes for the last cycle at each rate are plotted versus the effective C-rate in Figure 10. This quantity is defined by $C = I_A/Q_{Exp}$ where I_A is the applied current (mA g^{-1}) and Q_{Exp} is the experimental capacity which is lower than the theoretical one (Q_{Th} = 335 mA h

---

(39) Zhang, H.; Li, G. R.; An, L. P.; Yan, T. Y.; Gao, X. P.; Zhu, H. Y. *J. Phys. Chem. C* **2007**, *111*, 6143.

(40) Inaba, M.; Oba, Y.; Niina, F.; Murota, Y.; Ogino, Y.; Tasaka, A.; Hirota, K. *J. Power Sources* **2009**, *189*, 580.

(41) An, L. P.; Gao, X. P.; Li, G. R.; Yana, T. Y.; Zhub, H. Y.; Shen, P. W. *Electrochem. Acta* **2008**, *53*, 4573.

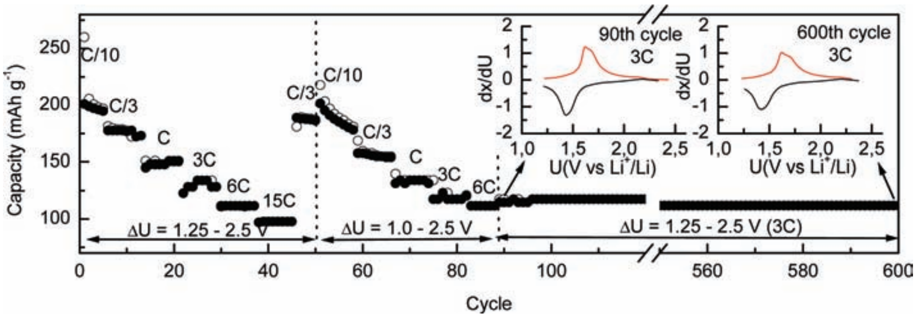

Figure 9. Variation in charge (open circles) and discharge (filled circles) at different cycling rates performed on TiO_2(B) nanoribbons annealed at 500 °C during 3 h. The TiO_2(B)/carbon black/PVDF composition of the electrode is 44:50:6 in weight ratio. The cells were cycled in 1 M $LiPF_6$ EC/DEC 1:1 electrolyte versus a metallic lithium electrode in the 1.25−2.5 voltage range between the first and the 50th cycle and between the 89th and the 600th cycle, and in the 1.0−2.5 voltage range between the 50th and the 88th cycle. The cycling rate between the 89th and the 600th cycle is 3C. The two insets show the incremental capacity during the 90th (left) and the 600th (right) cycles. Capacity is given per weight of TiO_2(B) active material in the electrode.

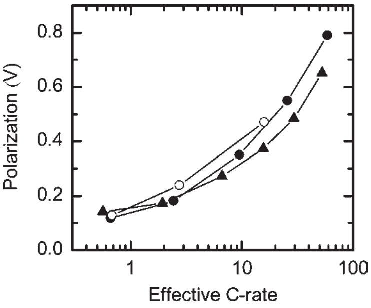

Figure 10. Comparison of the polarization for the three electrodes extracted from the last cycle of each speed rate. Open circles, filled circles, and triangles refer to the unpressed 70:24:6, to the 8 kbar pressed 70:24:6, and to the 44:50:6 weight ratio electrodes, respectively.

g^{-1}). The different trace shapes, although close for the three electrodes, depict a lower polarization for the highest carbon content thus suggesting that the isolating character of TiO_2(B) can be counterbalanced by adequate mixing with carbon additives, and this can be a research direction in the future for optimizing active material to carbon ratio in the composite electrode. Thus, the capacity differences between the three electrodes seem to be related to the number of electrically accessible TiO_2(B) nanoribbons, which is higher if the electrode is pressed and much higher for the 50 wt % carbon black electrode. It might be possible that the small distortions of TiO_2(B) particles with insertion/deinsertion of lithium ions isolate some crystallites from the carbon black, especially when the carbon black load is low. Indeed, the difference in particle size and shape between carbon black and TiO_2(B) as well as the trend to agglomerate as bundles for titanate nanoribbons require the use of a large amount of carbon black to connect each of the nanoribbons. This is also supported by the calculation of the electronic conductivity for a composite electrode composed of small nanoribbons and bigger carbon black spheres.[42] Thus, the high power density of nanosized material is no longer limited by lithium bulk diffusion, but by the electrical and ionic conductivities between active particles.

TiO_2(B) nanoribbons appear appropriate for high power and long life anode in lithium ion batteries but efforts on nanostructured architectures have to be done to improve electrical and ionic conducting networks, as already demonstrated in the literature, not only for titanates,[43,44] but also for germanium[45] based electrodes, VO_2 ultrathin nanowires[46] or $LiFePO_4$ nanoplates.[47,48]

Conclusion

Nanosized TiO_2(B) has been investigated as a possible candidate to replace $Li_4Ti_5O_{12}$ or graphite as a negative electrode material for Li-ion battery. The synthesis is close to the process reported by Kasuga et al.: the reaction is carried out in concentrated alkaline solution under reflux at 120 °C. Temperatures above 170 °C are generally required under autogenous conditions in autoclaves to produce nanoribbons. We prove that reflux enables the formation of nanoribbons too, with smaller thickness (6 nm) conducting to a high specific surface area ($S_{BET} \sim 140$ m^2 g^{-1}). They mainly transform in TiO_2(B), after annealing at 500 °C during 3 h with a very low anatase content estimated at 5% by Raman spectroscopy and high specific surface area (115 m^2 g^{-1}). Thermal treatment at high temperature and long plateaus facilitate the dehydration and the crystallinity of TiO_2(B). In addition, in lithium batteries, the polarization remains small, and high lithium ion insertion (up to $Li_{0.84}TiO_2$ during the first discharge) is promoted. Thin TiO_2(B) nanoribbons exhibit interesting rate capabilities (Q_{rev} = 100 mA h g^{-1} at 15C) and cycleability. They appear appropriate for a high power and long life anode in lithium ion batteries, but efforts on nanostructured architectures have to be done to improve electrical and ionic conducting networks, as already demonstrated in the literature.

Acknowledgment. The authors thank S. Grolleau for the TGA-MS experiments. They also thank ANR-PV and CNRS for financial support. T. Beuvier also thanks the CNRS and Total for his Ph.D. grant.

---

(42) Guoping, W.; Qingtang, Z.; Zuolong, Y.; Mei Zheng, Q. *Solid State Ionics* **2008**, *179*, 263.

(43) Ren, Y.; Hardwick, L. J.; Bruce, P. G. *Angew. Chem., Int. Ed.* **2010**, *49*, 2570.

(44) Saravanan, K.; Ananthanarayanan, K.; Balaya, P. *Energy Environ. Sci.* **2010**, *3*, 939–948.

(45) Cui, G.; Gu, L.; Kaskhedikar, N.; van Aken, P. A.; Maier, J. *Electrochim. Acta* **2010**, *55*, 985.

(46) Armstrong, G.; Canales, J.; Armstrong, R. A.; Bruce, P. G. *J. Power Sources* **2008**, *178*, 723.

(47) Gaberscek, M.; Dominko, R.; Bele, M.; Remskar, M.; Jamnik, J. *Solid State Ionics* **2006**, *177*, 3015.

(48) Suravanan, K.; Vittal, J. J.; Reddy, M. V.; Chowdari, B. V. R.; Balaya, P. *J. Solid State Electrochem.* **2010**, *14*, 1755.

Supporting Information Available: Raman spectra of titanic acids after annealing (Figure S1), position of the acid-treated titanate in a morphology diagram nanosphere/nanotube/nanoribbon (Figure S2), observed, calculated, and difference powder XRD profile after exchange and annealing at 400 °C for 3 h, 24 h and at 500 °C for 3 h (Figure S3), crystallographic parameters and calculated density of sample annealed at 500 °C for 3 h (Table S1), scanning electron micrograph of TiO_2(B) (Figure S4), initial charge−discharge curves at C/48 (I_{Appl} = 7.0 mA.g^{-1}) of nanosized TiO_2(B) (Figure S5), TGA traces after annealing at 400 °C for 24 h and 500 °C for 3 h (Figure S6), and charge−discharge curves of the eighth cycle of each rate of nanosized TiO_2(B) (Figure S7). This material is available free of charge via the Internet at http://pubs.acs.org.